Large-Eddy Simulation of Unsteady Wall Heat Transfer in a High Pressure Combustion Chamber

Nathalie Tramecourt,[*] Matthieu Masquelet[†] and Suresh Menon[‡]

Georgia Institute of Technology,

School of Aerospace,

Atlanta, GA, 30332-0150,

USA

This paper is composed of two parallel studies. The first one aims at predicting the unsteady heat flux at the wall of a rocket combustion chamber. In order to capture the unsteady nature of the wall heat transfer, Large Eddy Simulation is used. Peaks of heat fluxes are observed at different locations in the chamber. These peaks are observed to correspond to regions of vortex pairing and growth. On average, our simulation underpredicts the amount of heat to be transferred to the wall. Several explanations are suggested in the paper. The second study focuses on the influence of the thermodynamic and transport properties on the wall heat transfer. Comparisons between thermally perfect and real gas models are conducted and results highlight the importance of the choice of the model.

I.   Introduction

Over the years, interest in time accurate studies of rocket motor combustion has been driven by the need to reduce the cost of development of propulsion systems. Numerical simulations are only recently becoming feasible due to the advent of massively parallel computers. In the past, steady state studies[1, 2, 3] have been numerous, but unsteady simulations have been very rare. Recent unsteady simulations include the axisymmetric Large Eddy Simulation (LES) studies of supercritical mixing,[4] and the more recent rocket motor studies of single injector configurations.[5, 6, 7] In these latter studies, the limited size of the domain of interest allowed simulation of Liquid Oxygen (LOX) injection under sub-critical conditions for which a very high resolution was required due to the large density gradients. Thus, the three-dimensional (3D) computational domain used by Oefelein[6, 7] needed around 12 million grid points for a single, small-scale injector. This computational requirement is prohibitive for design studies where many simulations need to be carried out for parametric analysis.

Although these studies gave interesting insights into the behavior of the flow in a realistic high pressure environment, they did not address the transfer of heat to the walls of the combustion chamber. The wall heat transfer is a very important issue for both rocket engines and gas turbines. In a modern rocket engine, heat fluxes can reach more than 100 MW/m^2 at the throat of the chamber. Cooling is necessary to enforce a temperature below a certain value in order to avoid altering the liner material. But too much cooling will

---

[*]Graduate Research Assistant, AIAA Student Member
[†]Graduate Research Assistant, AIAA Student Member
[‡]Professor, and AIAA Associate Fellow

also effect the life cycle of the chamber. An accurate prediction of the amount of heat transferred to the walls of the chamber is then necessary. However, this phenomenon is highly unsteady and many challenges have to be addressed in a numerical simulation. The large temperature gradients at the wall require a very fine resolution that increases the computational cost. Also, the heat flux is drastically increased by turbulent heating and is intrinsically linked to turbulence modeling.

This paper uses Large-Eddy Simulation (LES) in order to address some of the issues related to the unsteadiness of the heat flux. Two studies are performed. First, a thermally perfect (TPG) study of the Penn State sub-scale $GOX - GH_2$ rocket engine is carried out. Even though the pressure in the chamber is higher than the critical pressure of the gases, the inflow temperature is such that the compressibility is unity. Under these conditions, there is no need to use the real gas formulation. A second study concerns the cryogenic injection of LOX in GH_2. The real gas (RG) formulation is now required as supercritical effects are expected to be important. A comparative study of thermally perfect gas versus real gas is carried out with a focus on the predicted heat flux and flow features.

II.   Governing Equations and Numerical Methods

A.   LES governing equations

The governing equations for LES are obtained by applying a spatial top hat filter (based on the grid size $\overline{\Delta}$) to the compressible Navier-Stokes equations for the mass, momentum, energy and species conservation. The use of Favre averaging is common in the study of compressible flow, and the filtered variable is defined by $\tilde{f} = \overline{\rho f}/\overline{\rho}$, where the over-line stands for spatial filtering. The resulting axisymmetric conservative equations are given by:

$$
\frac{\partial}{\partial t}
\begin{pmatrix}
\bar{\rho} \\
\bar{\rho}\tilde{u}_x \\
\bar{\rho}\tilde{u}_y \\
\bar{\rho}\tilde{E} \\
\bar{\rho}\tilde{Y}_k
\end{pmatrix}
+ \frac{\partial}{\partial x}
\begin{pmatrix}
\bar{\rho}\tilde{u}_x \\
\bar{\rho}\tilde{u}_x\tilde{u}_x + \bar{p} - (\tilde{\tau}_{xx} - \tau_{xx}^{sgs}) \\
\bar{\rho}\tilde{u}_x\tilde{u}_y - (\tilde{\tau}_{xy} - \tau_{xy}^{sgs}) \\
\bar{\rho}\tilde{u}_x\tilde{H} - \tilde{u}_x(\tilde{\tau}_{xx} - \tau_{xx}^{sgs}) - \tilde{u}_y(\tilde{\tau}_{xy} - \tau_{xy}^{sgs}) + \bar{q}_x + H_x^{sgs} + \sigma_x^{sgs} \\
\bar{\rho}\tilde{u}_x\tilde{Y}_k - \bar{\rho}\tilde{Y}_k\tilde{V}_{x,k} + Y_{x,k}^{sgs} + \theta_{x,k}^{sgs}
\end{pmatrix}
$$

$$
+ \frac{1}{y}\frac{\partial}{\partial y}
\begin{pmatrix}
\bar{\rho}\tilde{u}_y\,y \\
\bar{\rho}\tilde{u}_y\tilde{u}_x y - (\tilde{\tau}_{xy} - \tau_{xy}^{sgs})y \\
\bar{\rho}\tilde{u}_y\tilde{u}_y y + \bar{p} - (\tilde{\tau}_{yy} - \tau_{yy}^{sgs})y \\
(\bar{\rho}\tilde{u}_y\tilde{H} - \tilde{u}_x(\tilde{\tau}_{xy} - \tau_{xy}^{sgs}) - \tilde{u}_y(\tilde{\tau}_{yy} - \tau_{yy}^{sgs}) + \bar{q}_y + H_y^{sgs} + \sigma_y^{sgs})y \\
(\bar{\rho}\tilde{u}_y\tilde{Y}_k - \bar{\rho}\tilde{Y}_k\tilde{V}_{y,k} + Y_{y,k}^{sgs} + \theta_{y,k}^{sgs})y
\end{pmatrix}
=
\begin{pmatrix}
0 \\
0 \\
-\frac{(\tilde{\tau}_\theta - \tau_\theta^{sgs})}{y} \\
0 \\
\dot{\bar{\omega}}_k
\end{pmatrix}
\tag{1}
$$

Here, (x, y) represent respectively, streamwise and radial directions. Equations (1) neglect any motion in the circumferential direction. Here, ρ, u, v, E and Y_k represent respectively, the mixture density, the axial velocity, the radial velocity, the total energy and the mass fraction of species k. Also, H represents the total enthalpy $H = E + p/\rho$. The species equation has been written for the kth species, with k varying between 1 and N_S, the total number of species. Also, τ_{ij} represents the viscous stress tensor obtained in terms of the filtered variables:

$$
\tau_{xx} = \frac{4}{3}\bar{\mu}\frac{\partial \tilde{u_x}}{\partial x} - \frac{2}{3}\bar{\mu}\left(\frac{\partial \tilde{u_y}}{\partial y} + \frac{\tilde{u_y}}{y}\right)
\tag{2}
$$

$$
\tau_{yy} = \frac{4}{3}\bar{\mu}\frac{\partial \tilde{u_y}}{\partial y} - \frac{2}{3}\bar{\mu}\left(\frac{\partial \tilde{u_x}}{\partial x} + \frac{\tilde{u_y}}{y}\right)
\tag{3}
$$

$$
\tau_{xy} = \tau_{yx} = \bar{\mu}\left(\frac{\partial \tilde{u_y}}{\partial x} + \frac{\partial \tilde{u_x}}{\partial y}\right)
\tag{4}
$$

where μ is the molecular viscosity coefficient. τ_θ represents a viscous stress that arises because of the

axisymmetric formulation:

$$\tau_\theta = \frac{4}{3}\bar{\mu}\frac{\tilde{u_y}}{y} - \frac{2}{3}\bar{\mu}\left(\frac{\partial \tilde{u_x}}{\partial x} + \frac{\partial \tilde{u_y}}{\partial y}\right) \tag{5}$$

The heat flux vectors are given by:

$$\bar{q}_i = -\bar{\kappa}\frac{\partial \tilde{T}}{\partial x_i} + \bar{\rho}\sum_{k=1}^{N_s}\tilde{h}_k\tilde{Y}_k\widetilde{V_{i,k}} + \sum_{k=1}^{N_s}q_{i,k}^{sgs} \tag{6}$$

and the diffusion velocities are approximated using Fickian diffusion as:

$$\widetilde{V_{i,k}} = -\frac{\bar{\mathcal{D}}_k}{\tilde{Y}_k}\frac{\partial \tilde{Y}_k}{\partial x_i} \tag{7}$$

The pressure is determined from the filtered equation of state. Depending on the temperature and pressure conditions in the combustion chamber, a different equation of state is necessary to describe the behavior of the flow. A general form containing the compressibility factor Z is used in this section and will be further explained in the next sections. The equation of state is written $p = Z\rho RT$. In the case of thermally perfect gases (TPG), Z is 1 and the equation of state reduces to the well known $p = \rho RT$. The filtered form of the real gas equation of state is:

$$\bar{P} = \bar{\rho}R_u\sum_{k=1}^{n}(\frac{\tilde{Z}\tilde{Y}_k\tilde{T}}{W_k}) + \bar{\rho}R_u\sum_{k=1}^{n}(\frac{\widetilde{ZY_kT} - \tilde{Z}\tilde{Y}_k\tilde{T}}{W_k}) \tag{8}$$

Here, R_u is the universal gas constant and W_k is the molecular weight for the k-th species. The first term on the right hand side contains only resolved values : $\tilde{Z}$, $\tilde{Y}_k$, $\tilde{T}$. The second term includes a triple correlation of the temperature, compressibility and species terms and is a term that requires closure. As mentioned earlier, for thermally perfect gases, the filtered equation of state is the same as Eqn. (8) except that $Z = 1$. It has been shown[8] that subgrid term in the above equation is negligible for low heat release in a perfect gas, and it seems to be also the case for real gases[9] even though this has not been clearly demonstrated for a reacting case as yet.

Several terms in the LES equations require closure:

$$\begin{aligned}
\tau_{ij}^{sgs} &= \bar{\rho}(\widetilde{u_i\,u_j} - \tilde{u}_i\tilde{u}_j) \\
H_i^{sgs} &= \bar{\rho}(\widetilde{E\,u_i} - \tilde{E}\tilde{u}_i) + (\overline{p\,u_i} - \bar{p}\tilde{u}_i) \\
\sigma_i^{sgs} &= \widetilde{u_j\,\tau_{ij}} - \tilde{u}_j\tilde{\tau}_{ij} \\
Y_{i,k}^{sgs} &= \bar{\rho}(\widetilde{u_i\,Y_k} - \tilde{u}_i\tilde{Y}_k) \\
q_{i,k}^{sgs} &= \overline{h_k\,D_k\,\partial Y_k/\partial x_i} - \tilde{h}_k\tilde{D}_k\partial\tilde{Y}_k/\partial x_i \\
\theta_{i,k}^{sgs} &= \bar{\rho}(\widetilde{V_{i,k}\,Y_k} - \tilde{V}_{i,k}\tilde{Y}_k) \\
T_k^{sgs} &= \frac{\widetilde{ZY_kT} - \tilde{Z}\tilde{Y}_k\tilde{T}}{W_k}
\end{aligned} \tag{9}$$

They represent, respectively, the subgrid stress, the subgrid enthalpy flux, the subgrid viscous work, the subgrid species flux, the subgrid heat flux, the subgrid diffusive species flux and, the subgrid temperature-scalar correlation.

Here, a closure based on a transport model for the subgrid kinetic energy k^{sgs} ($k^{sgs} = \frac{1}{2}[\widetilde{u_ku_k} - \tilde{u}_k\tilde{u}_k]$) is used to close the momentum and energy subgrid fluxes, τ_{ij}^{sgs} and H_i^{sgs}, respectively. In this approach, a one-equation model for k^{sgs} is solved along with the LES equations:

$$\frac{\partial\bar{\rho}k^{sgs}}{\partial t} + \frac{\partial}{\partial x_i}\left(\bar{\rho}\tilde{u}_ik^{sgs}\right) = P^{sgs} - D^{sgs} + \frac{\partial}{\partial x_i}\left(\frac{\bar{\rho}\nu_t}{\sigma_k}\frac{\partial k^{sgs}}{\partial x_i}\right) \tag{10}$$

American Institute of Aeronautics and Astronautics Paper AIAA-2005-4124

Here, ν_t is the turbulent viscosity given as $\nu_t = C_\nu \sqrt{k^{sgs}} \ \overline{\Delta}$, and σ_k is a constant set to 1. Also, P^{sgs} is the subgrid kinetic energy production and D^{sgs} is the subgrid kinetic energy dissipation, and are defined as

$$P^{sgs} = -\tau_{ij}^{sgs} \frac{\partial \widetilde{u}_i}{\partial x_j} \tag{11}$$

$$D^{sgs} = C_\epsilon \overline{\rho} \frac{(k^{sgs})^{\frac{3}{2}}}{\overline{\Delta}} \tag{12}$$

Given ν_T, the subgrid stresses and energy flux are closed as follows:

$$\tau_{ij}^{sgs} = -2\overline{\rho}\nu_T \left(\widetilde{S_{ij}} - \frac{1}{3} \widetilde{S_{kk}} \delta_{ij} \right) + \frac{2}{3} \overline{\rho} k^{sgs} \delta_{ij} \tag{13}$$

$$H_i^{sgs} = -\overline{\rho} \frac{\nu_T}{Pr_t} \frac{\partial \widetilde{H}}{\partial x_i} \tag{14}$$

In the above equation, S_{ij} is the strain tensor, δ_{ij} is the Kronecker delta and Pr_t is the turbulent Prandtl number.

The subgrid viscous work, σ_i^{sgs} has been neglected in the past[10,11] . This assumption is justified in the case of a high Reynolds number flow, where the viscous terms are generally small compared to the convective terms. As a consequence, the viscous subgrid transport term is considered negligible. Earlier studies[12] have shown that the two model coefficients C_ν and and C_ϵ have constant values of 0.067 and 0.916. The derivation of those constants did not imply any assumptions of incompressibility or ideal gas behavior and are consequently used as is for both thermally perfect and real gas studies.

The mixture viscosity and thermal conductivity can be computed in two different ways. The first method uses the Sutherland law for the viscosity. It is well known that this law is strictly valid only for a single component substance. As a consequence, a more accurate computation of the mixture viscosity is performed by first computing the viscosity of the pure substances using the Sutherland's law and then combining them following Wilke's formulation.[13] The thermal conductivity can be computed from the definition of the Prandtl number for the mixture or using the Wassiljewa equation,[14] which is equivalent to the Wilke's formula for the thermal conductivity. The influence of the computation of the thermal properties on the heat flux will be discussed in Section III.

B.   Real gas equation of state

In this studies, the cubic Peng-Robinson equation of state (PR-EOS) has been chosen. It is an acceptable choice from accuracy and cost considerations. Also, studies[15] have shown that the PR-EOS is the most accurate cubic equation for rocket motor application. It can also be applied to model sub-critical behavior due to its accuracy in the compressed liquid domain. The PR-EOS also reduces to the thermally perfect EOS when the conditions changes. As a consequence, no switch is required to simulate the flow behavior when Z is unity.

The mixing rules used are those employed by Miller[16] to define the mixture parameters A_m and B_m:

$$A_m = \sum_i \sum_j X_i X_j A_{ij} \qquad B_m = \sum_i X_i B_i \tag{15}$$

where R_u is the universal gas constant. The specific parameters of the PR-EOS are calculated as follows (the subscript c represents a critical property and the subscript r a reduced property, i.e., T/T_c):

$$A_{ij} = 0.457236 \frac{R_u^2 T_{c(ij)}^2}{P_{c(ij)}} \alpha(T_{c(ij)}) \tag{16}$$

$$\alpha(T_{c(ij)}) = \left[1 + f(\Omega_{ij}) \left(1 - \sqrt{T_{c(ij)}} \right) \right]^2$$

American Institute of Aeronautics and Astronautics Paper AIAA-2005-4124

$$f(\Omega_{ij}) = 0.37964 + 1.48503\Omega_{ij} - 0.164423\Omega_{ij}^2 \tag{17}$$

$$B_i = 0.07779\frac{R_u T_{c(ii)}}{P_{c(ii)}} \tag{18}$$

where Ω is the accentric factor. The combining rules for the critical properties are:

$$
\begin{aligned}
T_{c(ij)} &= (1 - k_{ij})\sqrt{T_{c(i)}T_{c(j)}}, \;\; P_{c(ij)} = Z_{c(ij)}\frac{R_u T_{c(ij)}}{V_{c(ij)}} \\
V_{c(ij)} &= \tfrac{1}{8}\left(V_{c(i)}^{1/3} + V_{c(j)}^{1/3}\right)^3, \;\; Z_{c(ij)} = \tfrac{1}{2}(Z_{c(i)} + Z_{c(j)}) \\
\Omega_{(ij)} &= \tfrac{1}{2}(\Omega_{(i)} + \Omega_{(j)})
\end{aligned}
\tag{19}
$$

where k_{ij} is a constant binary interaction parameter.

Details of the computation of the thermodynamic and transport properties, as well as the iterative process performed in the main solver to compute temperature and pressure from density and energy are not detailed here, for brevity. The transport properties are computed using the methodology developed earlier[17] for high pressure gases, which is considered most effective in terms of computational cost and accuracy.[15] The iterative process is similar to the one described by Okong'o et al.[18]

C.   Numerical methods

The governing equations are solved using a finite volume, predictor-corrector scheme, that is second-order accurate in time and fourth-order accurate in space. This solver is implemented in parallel using the MPI library.

1.   Thermally Perfect Study

Figures 1 shows the full computational domain and the grid used for the thermally perfect rocket simulations close to the injector plate. Table 1 summarizes the dimensions for the different injectors. Table 2 summarizes the test conditions and nominal inflow conditions used in this study. Oxygen is injected through the central post and hydrogen is injected through the outer injector. The Δy in the hydrogen channel is of the order of 25 microns and is around 37 microns in the oxygen channel. The grid near the injectors is nearly uniform and is slowly stretched away from the injector region. The maximum grid stretching is 5% axially and 9% radially. The total grid resolution is 776×181 for the TPG rocket simulations. The large number of axial grid points is due to the length of the domain.

Exit O_2 channel radius	2.63 mm
Exit O_2 channel grid points	38
Tip wall width	0.52 mm
Tip wall grid points	20
H_2 channel width	0.597 mm
H_2 channel grid points	27

Table 1.   Physical and computational dimensions of the different parts of the injectors for the PSU rocket chamber.

The outflow is supersonic and therefore, extrapolation is used at the outflow plane. Characteristic-based constant mass flux subsonic boundary conditions are used at the inflow for both the injectors (the mass flux as well as the temperature is imposed, the rest is recomputed). We implement an isothermal, non catalytic,
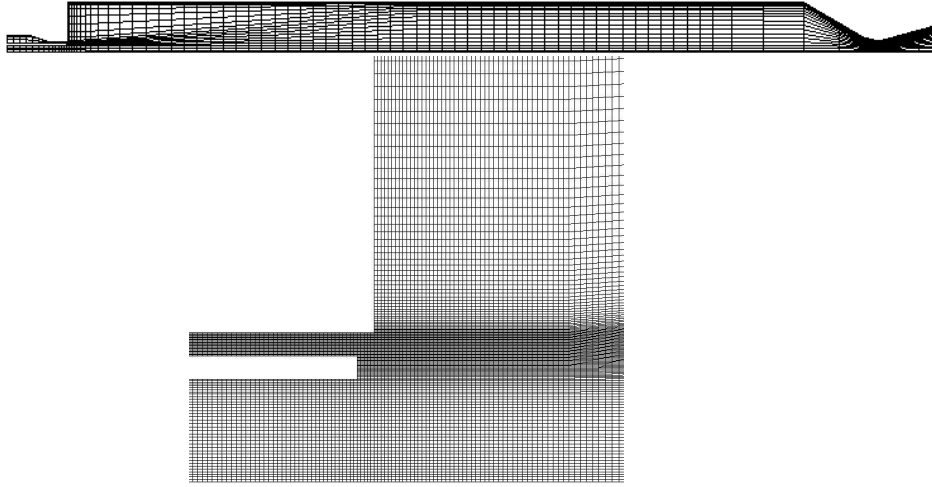
Figure 1. Global view of the grid (top) and Grid near the injection plane (bottom) for the PSU rocket study case.

	O_2 channel	H_2 channel
T (K)	767	798
Mass Flow rate (Kg.s^{-1})	0.0327	0.0896
Mass fraction of O_2	0.9462	0
Mass fraction of H_2	0	0.4130
Mass fraction of H_2O	0.0538	0.5870

Table 2. Test conditions for the PSU rocket chamber.

no-slip condition on the combustor top so that the temperature at the interface between the flow cell and the ghost cell remains constant through time, assuming a parabolic profile for the temperature gradient at the wall. For a uniform grid at the wall, this profile results in:

$$\left(\frac{\partial T}{\partial y}\right)_{wall} = \frac{-9T_j + 8T_{wall} + T_{j-1}}{3\Delta y} \tag{20}$$

The ghost cell temperature is then obtained from this temperature gradient. Figure 2 shows the experimental temperature profile imposed on this wall. Following Poinsot,[19] a nearly-isothermal law-of-the-wall model is implemented, to compute the turbulent kinetic energy in the near wall region.

The dump plane of the chamber also has isothermal, non catalytic wall boundary conditions. The temperature at the wall goes from $750\ K$ at the junction with the upper wall to $900\ K$ at the injector periphery. The same parabolic profile for the temperature gradient at the wall is applied but in the x-direction. The other walls (e.g. the injector walls) are no-slip adiabatic.

2. Real Gas Study

The real gas EOS involves a lot of complex operations such as real-powers, square roots, logarithms, etc. More than 20% of the CPU time is used for these operations. The computation of the transport properties computations also require similar operations. Analysis showed that these properties vary very slowly with
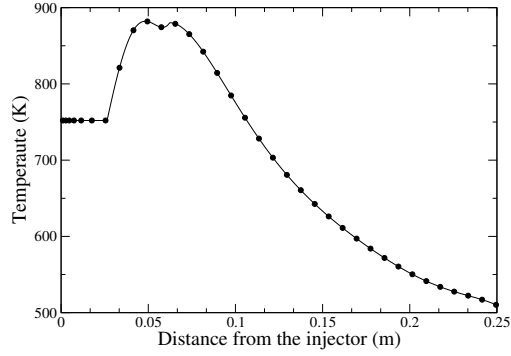
American Institute of Aeronautics and Astronautics Paper AIAA-2005-4124

Figure 2. Plot of the experimental temperature imposed on the upper wall.

time, and in the current combustion study, were computed every three steps to reduce the computational cost. The overall error of doing this simplification is less than 0.1%.

Figure 3 shows the grid used for the real gas rocket simulations close to the injector plate while Table 3 gives the precise dimensions for the different injectors. This configuration simulates three injectors instead of the single one in the TPG study. The tip walls between the oxygen and hydrogen channels are resolved with around 7 points, as are the hydrogen channels. Due to the small dimensions (less than half a millimeter) of these channels, this resolution leads to a Δy of the order of 50 microns. Near the motor wall a grid resolution of $\Delta y = 20$ microns is used. The grid near the injectors is nearly uniform and is slowly stretched away from the injector region. The maximum grid stretching is also 5% axially and 9% radially. Earlier, some grid resolution issues were investigated primarily to ensure that all the features near the injector lips are well resolved. Based on these studies, we employ a grid of 436×362 for all the reported RG/TPG comparison studies.

	Centerline injector	Outer injectors
Initial O_2 channel radius	2.8643 mm	1.129 mm
Initial O_2 channel grid points	26	16
Exit O_2 channel radius	3.15 mm	1.8604 mm
Exit O_2 channel grid points	26	16
Tip wall width	0.325 mm	0.325 mm
Tip wall grid points	6	6
Lower H_2 channel width	None	≈ 0.444 mm
Lower H_2 channel grid points	None	7
Upper H_2 channel width	0.585 mm	≈ 0.386 mm
Upper H_2 channel grid points	9	6

Table 3. Physical and computational dimensions of the different parts of the injectors for the RG rocket

The same no-slip, isothermal, non catalytic boundary conditions are applied at the upper wall of the combustion chamber. Figure 5 shows the imposed temperature profile. All other walls are no-slip adiabatic.

D.   Chemistry

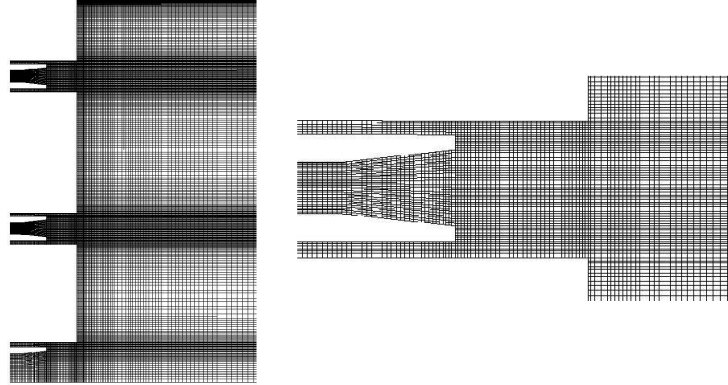The following two-step reduced mechanism is used for all the combustion studies:[20]

American Institute of Aeronautics and Astronautics Paper AIAA-2005-4124

Figure 3. Grid of the three injectors for the RG rocket study case (left) and close-up on one injector (right).

$$H_2 + O_2 \rightleftharpoons 2\,OH \tag{21}$$
$$2\,OH + H_2 \rightleftharpoons 2\,H_2O \tag{22}$$

The forward reaction rates are computed from the Arrhenius law:

$$k_{f_1} = A_1 T^{-10} e^{-4865/R^0 T} \tag{23}$$
$$k_{f_2} = A_2 T^{-13} e^{-42,500/R^0 T} \tag{24}$$

where

$$A_1 = (8.917\phi + 31.433/\phi - 28.95)(10^4 7)\ cm^3/mol.s \tag{25}$$
$$A_2 = (2.0 + 1.333/\phi - 0.833\phi)(10^6 4)\ cm^6/mol^2.s \tag{26}$$

and

$$K_1 = 26.164 \exp^{-8992/T} \tag{27}$$
$$K_2 = 2.682 \times 10^{-6} T \exp^{69415/T} \tag{28}$$

However, in order to limit the mean reaction rate, the Arrhenius law is coupled with the subgrid Eddy Break-Up (EBU) model.[21] The idea behind the EBU model is that the rate of combustion is determined by the rate at which parcels of unburned gas are broken down into smaller ones. So turbulent motions control the reaction rate. In order to couple the EBU model with the Arrhenius law, the reaction rate is taken as the minimum between the chemical rate and the turbulent mixing rate.
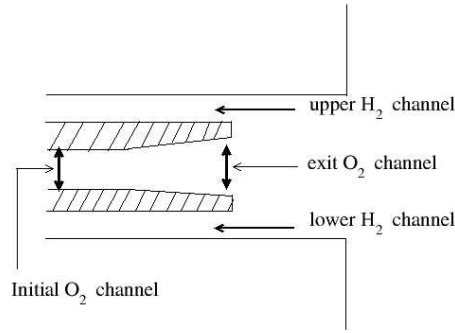
American Institute of Aeronautics and Astronautics Paper AIAA-2005-4124

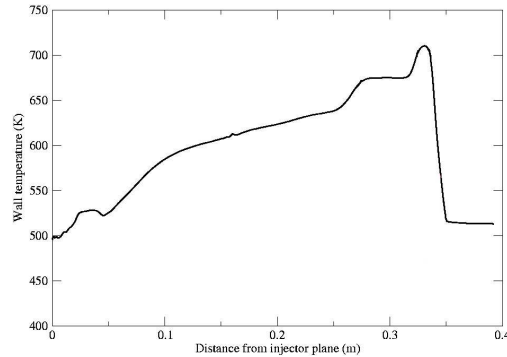**Figure 4. Names of the channels for Table 3**

Figure 5. Wall temperature profile for the RG/TPG rocket study.

III.   Results and Discussion

A.   Thermally perfect study of a rocket engine combustion chamber

1.   Flow field features

Figure 6 shows the instantaneous and steady state temperature in the combustion chamber. Due to the axisymmetric formulation, no radial momentum perturbs the jet through the centerline. This explains why the jet remains along the centerline and shows no flapping motion characteristic to the coaxial injection. As a consequence less mixing occurs in the chamber. This formulation also results in a longer jet as in a full 3D simulation. Significant unsteady vortex shedding can be seen in the mean field. By around five diameters, these shed structures are large enough to reach the centerline, denoting the end of the potential core of the oxygen jet. This can be seen on the steady state figure where the low temperature region coming from the oxygen channel ends.

The flame can be observed in Fig. 7. Here, we see that the hydrogen jet rolls up more than the oxygen one. This is a direct consequence of the density ratio at the injection stage (about 30 Kg/m^3 for the oxygen and 4.5 Kg/m^3 for the hydrogen). Also, even though the resolution is very fine close to the injector in both the directions, the flame shows some discontinuity two diameters downstream. If this is not a major issue in this case, it could lead to some instabilities if the real gas formulation were used. Indeed, in an environment were the real gas formulation has to be used, thermal properties exhibit such large gradients
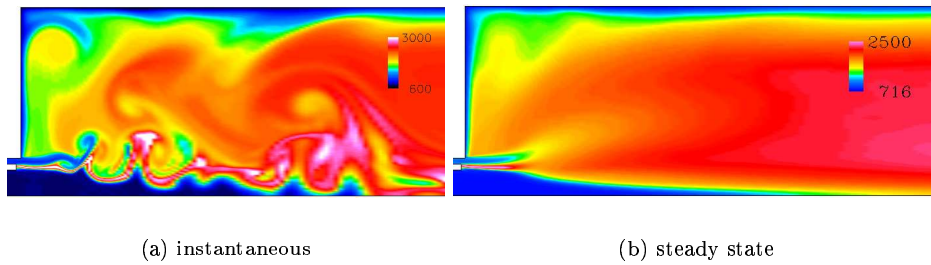
American Institute of Aeronautics and Astronautics Paper AIAA-2005-4124

(a) instantaneous   (b) steady state

Figure 6. temperature distribution near the injection plane for the PSU rocket study case.

that discontinuities in the interface create important instabilities. For the TPG study, this discontinuity is not a big issue. The steadu state evolution of the OH mass fraction shows only little penetration of the OH in the upper region of the combustor. This will be discussed later.
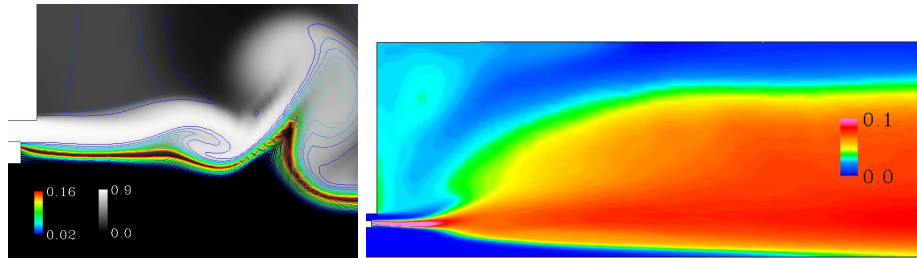

Figure 7. Left: H_2 mole fraction (gray scale) and OH mole fraction (lines) for the PSU rocket study case. Right: steady state OH mole fraction.

Due to the fine resolution in the injector region, a nice recirculation region is seen at the tip of the injector, as shown in Fig. 8. The oxidizer is transported upward toward the hydrogen jet and the flame anchors in the region of reverse flow. This flame holding may not be properly captured if a coarser grid is employed here.

Figure 9 shows the OH mole fraction and the distribution of turbulent kinetic energy in the domain. The region of high turbulent kinetic energy correspond to the region where the combustion is controlled by the mixing. In general, the highest concentration of OH is found in regions where the turbulent kinetic energy is low and is then transported upward by the vortical structures. The reaction rates are then mostly limited by the chemical rate.

2. *Unsteady Heat flux*

The transfer of heat to the wall of the combustion chamber is a highly unsteady process. This feature is highlighted in Fig. 10. In this figure, we show the distribution of the wall heat flux at four different non-dimensional times. The non-dimensional time t^* is defined as $t* = \Delta t/t_{FTT}$ where t_{FTT} is the flow-through-time and Δt represent the elapsed time between the beginning of the flow-through-time and the

American Institute of Aeronautics and Astronautics Paper AIAA-2005-4124
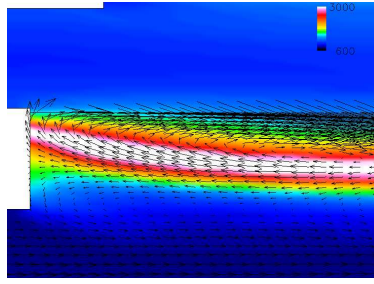
Figure 8. Temperature (color) and velocity vector at the tip of the injector for the PSU rocket study case.
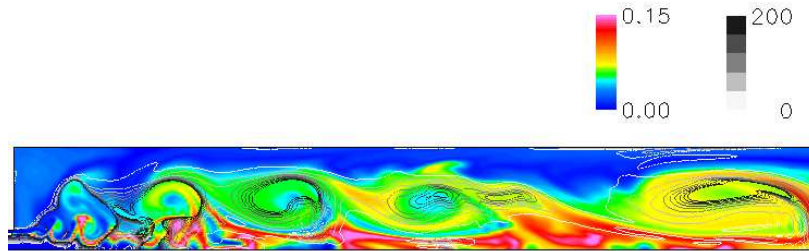

Figure 9. OH mole fraction (color) and turbulent kinetic energy distribution (lines) for the PSU rocket study case.

snapshot. At $t* = 0.054$, three peaks of heat flux of lesser intensity appear. They can also be related to the location of large vortical structures in the chamber. Fig 11 also displays the vorticity field at the same $t*$. At $t* = 0.032$, a peak at 9 $MW.m^{-2}$ is observed when the three other plots show values around 5 $MW.m^{-2}$ for the same location. This peak corresponds to the intermittent entrainment of hot product toward the wall in the recirculation region formed at the dump plane. At $t* = 0.3$, the heat flux peaks at about 22 $MW.m^{-2}$ at a distance of about 0.05m from the injector, and the peak to peak magnitude at this time reaches 20 $MW.m^{-2}$. This axial distance corresponds to the location where two vortices generated by the coaxial injection pair-up and get close to the top wall. This pairing of the vortices can be observed in Fig. 11. It is the only location where such a peak has been observed upstream the throat.

The vortex creation and vortex pairing thus seem to play an important role in the time evolution of the wall heat transfer.

Figure 12 shows the axial distribution of the heat flux averaged over 2.5 flow-through-times versus the experimental data. Three simulations have been performed. One where the laminar viscosity and thermal conductivity are constant. Another where those quantities vary with temperature only. And finally, one where they vary with both the mixture and the temperature. It can be seen that these simulations substantially underpredict the amount of heat to be transferred to the wall. Several factors contribute to this result. The three simulations predict similar heat flux, when we expect large variations of the temperature and mixture composition at the wall. Analysis of this data show that nothing is really happening near the upper wall. Figure 13, representing the OH mole fraction and velocity vectors, we see that there is a large region near the wall were the concentration of OH is nearly zero. This region is characterized by very low velocities. This means that near the upper wall, the transfer of heat occurs more by conduction than convection. This can also be seen in Fig. 14, which shows the time-averaged velocity field. We see that the jet never really attaches to the combustor wall. In this figure, the color represents the steady state negative velocity regions
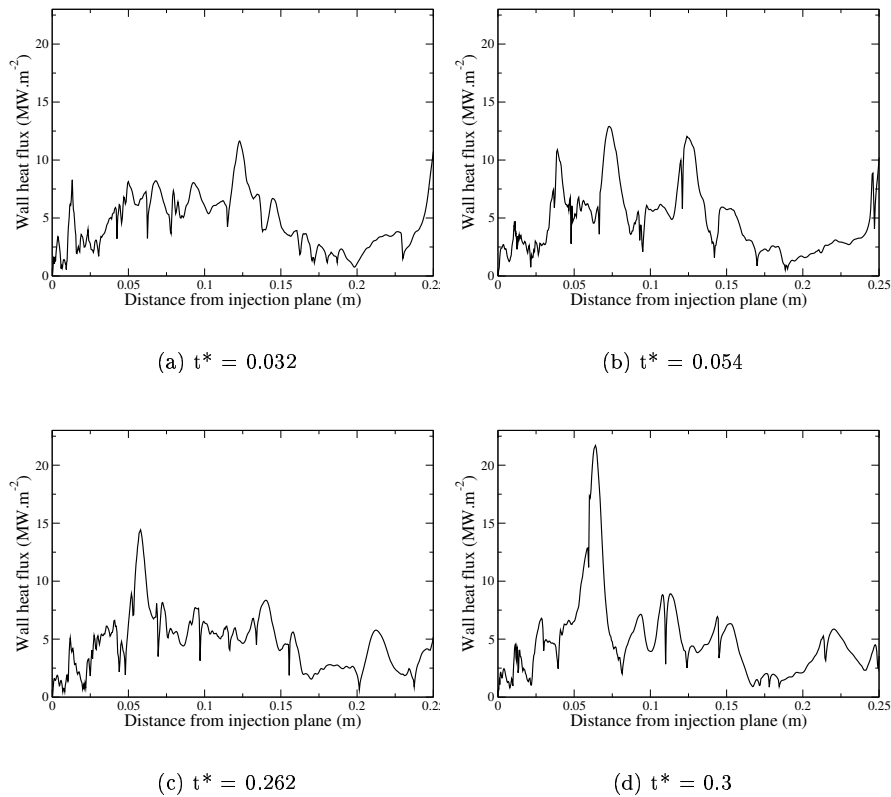
American Institute of Aeronautics and Astronautics Paper AIAA-2005-4124

(a) t* = 0.032

(b) t* = 0.054

(c) t* = 0.262

(d) t* = 0.3

Figure 10. Instantaneous heat flux at the wall at four different time.

in the combustor. We can see that the flow is positive in most of the chamber except near the top wall, where the counter-clockwise vortices entrain the flow toward the dump plane. This problem may be caused by the axisymmetric formulation that does not allow radial momentum through the centerline, and thus prevents the jet from flapping. This reduces the impingement of hot products on the wall. Another possibility is that the low velocity in this region implies that the turn around time for the flow here is very long, much longer than the current simulation. The resolution at the wall could also explain this low average heat flux. Even though the y^+ at the wall is around 6, parametric studies on the effect of the resolution have not yet been performed. Finally, it is worth noticing that the averaging time for the experiments is 0.4s whereas we average over 2.5 flow-through-times, which represents only 0.006s. Further contribution of this simulation is planned to see if the near-wall region will turn over to obtain more statistics.

B. Comparison of thermally perfect and real gas models

IV. Comparison of thermally perfect and real gas models

The comparison of the 2 equations of state is made here in the sub-scale, three injector rocket chamber described in Section C. Both runs are started from the same initial real gas solution. Since we have inlet boundary conditions that ensure that the mass flow-rate remains constant in time, the inflow conditions for both runs are similar in terms of flow-rate, temperature and mass fractions (note that, the system here is

American Institute of Aeronautics and Astronautics Paper AIAA-2005-4124
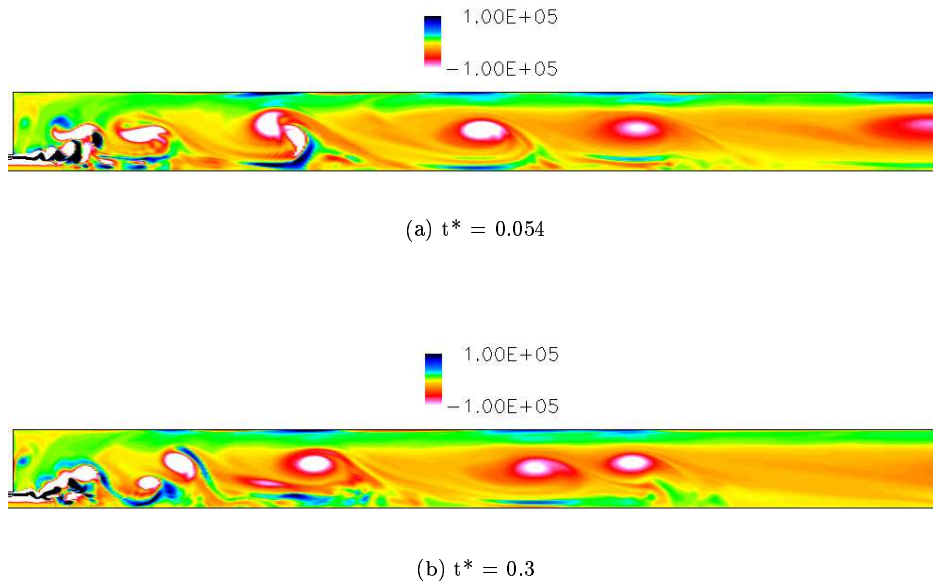
(a) t* = 0.054

(b) t* = 0.3

Figure 11. Instantaneous vorticity field.

non-premixed unlike the partially premixed PSU combustor). However, we expect the inlet densities and velocities to differ, especially for the oxygen jet which is injected under supercritical conditions for which its compressibility is significantly smaller than 1.

Both instantaneous and time-averaged mean flow properties were analyzed and some representative results are discussed below. For the instantaneous comparison, we have attempted to show characteristic figures that closely compare the flow features at (nearly) the same instant of flow development (identified here as the vortex shedding process from the injector lip).

In Fig. 15, we show the instantaneous oxygen concentration for both cases. One can clearly see the different behavior that occurs under the thermally perfect gas assumption. As stated before, the density of the oxygen jets is much lower for the TPG case (around 250 kg.m^{-3}) than for the RG case (around 380 kg.m^{-3}), and thus the inlet velocity for the oxygen is 50% higher in the TPG case. This of course has a direct impact on the dynamics of the jets since the velocity ratios have been changed. The breaking-up of the oxygen jets for the RG case seems to occur earlier than for the TPG, leading to large, round pockets of unburned oxygen being convected downstream. The oxygen jets in the TPG case appear thinner and extend further in the flow without pinching. As a result, although both jets seem to flap in a similar fashion, the jet in the TPG case will impinge the wall further away from the injector plate. This has a consequence on the wall heat flux. Furthermore, we can notice one of the shortcomings of our simulations in this figure by taking a closer look at the centerline jets. Because of the axisymmetric assumption, this jet is constrained to remain along its principal axis and cannot flap like the outer rows. Thus, we experience poor mixing along the centerline of the combustion chamber. The behavior is the same for both TPG and RG models: even the very different transport properties computed in both cases (inlet dynamic viscosities are about twice as large in the RG case) do not seem to have any influence on these constrained jets. Also, the Figure 15 for the RG case allows us to look at the extent of the real gas effects in the combustion chamber. As mentioned in Sec. C, the axisymmetric configuration and our assumptions to keep the velocity and momentum ratios
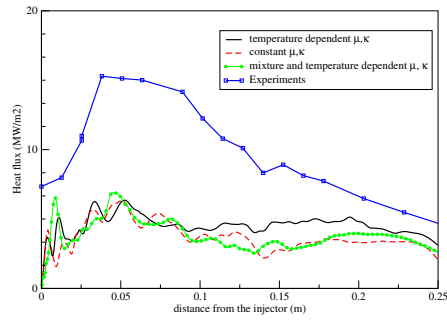
American Institute of Aeronautics and Astronautics Paper AIAA-2005-4124

Figure 12. Average heat flux at the wall over 2 flow through time.
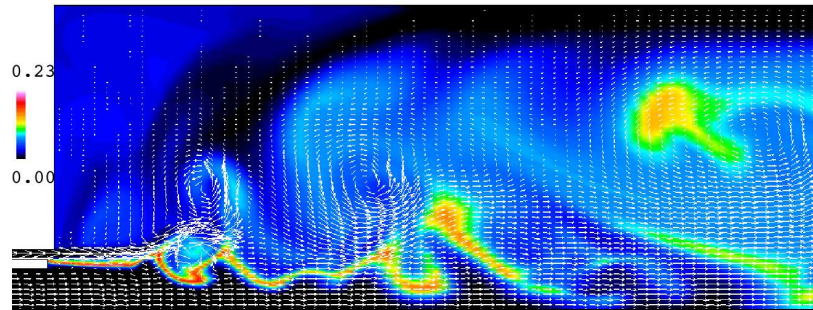

Figure 13. Instantaneous OH mole fraction (color) and velocity vectors.

close to the experimental values prevent us from having identical injectors. This explains why the real gas effects can be felt over a much larger region for the centerline injector. We even see that unburned pockets of oxygen, after having broken up from the jet, can experience significant departures from perfect gas behavior. This feature is not present in our simulation for the outer rows probably because their apparent diameter is smaller than what it should be in reality. For all jets, we can see that our RG model allows for a smooth transition between regions where the perfect gas model is not valid and where the compressibility is almost 1. Since the real gas model is very expensive in terms of computational resources, there is a need in the future to look at ways to bypass most of the RG computations when Z is sufficiently close to 1.

Figure 16 represents the temperature field in the near injector plate region (up to 20 centerline injector diameters downstream of the injection plane). Both fields present some similarities such as the temperature range displayed. As mentioned before, our boundary conditions make sure the injection temperatures are constant for both cases. Also, in both runs, the same 2-step reaction mechanism is used and thus yield similar flame temperatures. It has to be noted here that the computed enthalpies do differ in both models and that they induce a difference in flame temperature of about 100 K. For simplification, both scales on Fig. 16 are the same. With this scaling, it is easy to see that the flame, defined simply as the zone of highest temperatures, is almost continuous in the RG case, whereas multiple flame surfaces seem to coexist for the TPG case. This can be related to the previous analysis. It seems that the more regular pinching of the oxygen jets in the RG case allows the different pockets of oxygen to burn collectively. On the other hand, the thinner and longer oxygen jets in the TPG case each support one long flame which extends up to 15
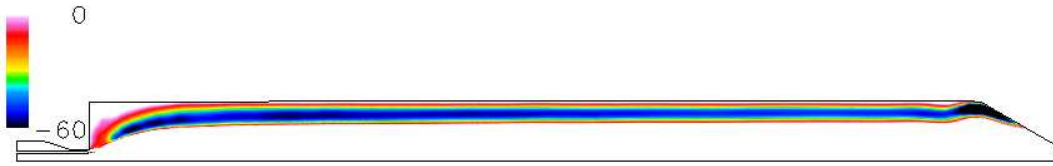
American Institute of Aeronautics and Astronautics Paper AIAA-2005-4124
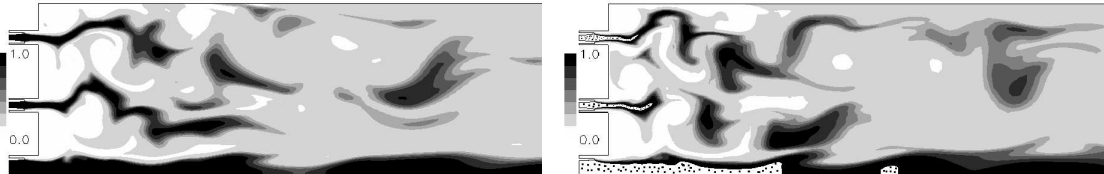
Figure 14. Steady state velocity field.

Figure 15. Instantaneous oxygen concentration fields for the TPG run (left) and RG run (right). The figure for the RG also includes a dotted area where the compressibility is in the range 0.6-0.9, i.e. where the real gas effects are significant.

diameters downstream. These flames are disconnected from each and from the more uniform combustion further downstream. A possible explanation is the higher thermal conductivity in the RG case than in the TPG case, which could facilitate the connection between the different flames. In order to investigate this, we run the TPG model using the transport properties from the RG model.

The average wall heat flux for both cases is shown in Fig. 17. Several features are interesting to discuss. First, the absolute level of heat flux, several tens of mega-watts per meter-square, is characteristic of those encountered in actual rocket engines. It is important that our simulations can represent such high values of heat transfer. Only looking at the laminar (or molecular) conduction of heat at the wall, such high rates of heat flux represent a temperature gradient of approximately 1000 K over 20 microns, the characteristic distance of our first cell center to the wall. This plot seems to show that for both RG and TPG models, the sub-grid model is able to capture at least part of the physics occurring along the wall chamber. Comparing both RG and TPG heat flux profiles, we can see that the peak value for the TPG model is higher and occurs further downstream compared to the RG simulation. This can be related to the jet dynamics described in the previous paragraphs which showed that the jet flapping is different between the two cases. This flapping causes the heat transfer to the wall to be a very transient phenomena. Finally, the profile obtained for the simulation using the TPG model with the real gas transport properties is also shown on Fig. 17. We can see once again the influence of the transport properties on the jets dynamics with the difference between the pure TPG profile and the mixed TPG/RG profile. The oxygen jets for this mixed case have less inertia than for the RG case but are more viscous than the pure TPG case. As a result, the oxygen jets are much more constrained by the hydrogen annulus and the flapping is reduced. Thus, the smaller value of the initial maximum on the heat flux profile. Even though this local behavior is different, we are still injecting the same quantity of reactants in the same conditions as for the TPG case. Since far downstream from the injection, the RG formulation and RG transport properties recover to their TPG counterpart, it is logical that the profiles for the TPG simulation and the mixed simulation are the same. For the RG, the lower inlet

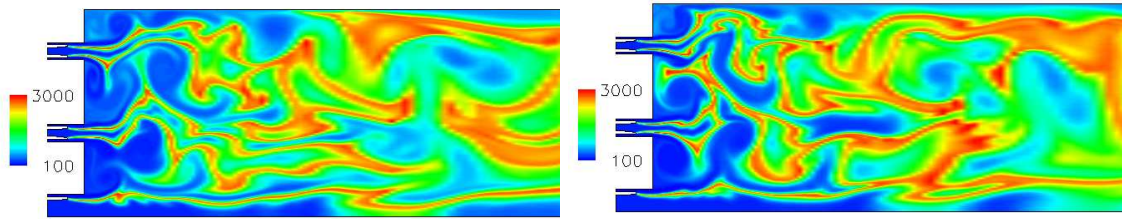American Institute of Aeronautics and Astronautics Paper AIAA-2005-4124

Figure 16. Instantaneous temperature fields for the TPG run (left) and RG run (right).
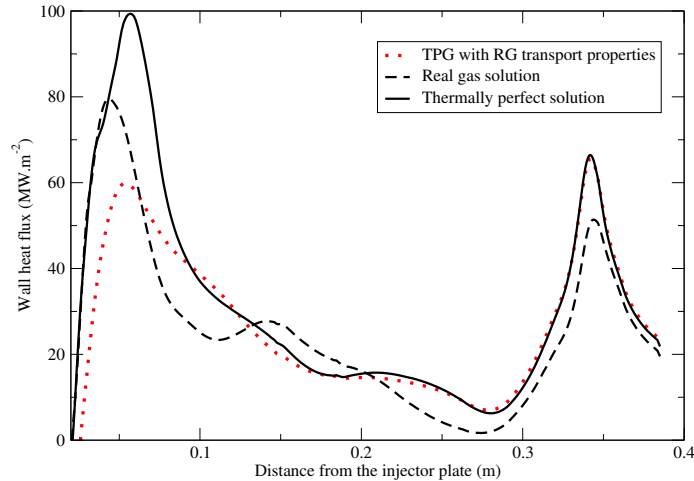

Figure 17. Time-averaged heat flux through the combustion chamber wall for the RG case (dashed line), the pure TPG case (full line) and the TPG case with RG transport properties (dotted line).

velocity for the oxygen seems to lead to less turbulent subgrid energy far downstream and thus to a lesser heat transfer in the later part of the chamber.

V.   Conclusion

Two parallel studies have been performed. The first study aims at predicting the unsteady heat flux at the wall of a rocket combustion chamber. The high temperature in the domain enables us to use the thermally perfect gases assumption even though the pressure in the chamber is over the critical pressure of the gases. The use of Large Eddy Simulation highlights the very unsteady nature of the wall heat transfer. The main chamber has to support very large thermal loads with heat fluxes that peak at more than 20 $MW.m^{-2}$. Also, this study reveals the correlation between instantaneous peaks of heat fluxes and vortex dynamics. Indeed, pairing is observed in the domain and peaks of heat flux correspond to location where large vortices transport hot products toward the wall. On an average, this simulation underpredicts the amount of heat to be transferred to the wall. The axisymmetric formulation may explain this discrepancy as it prevents the

American Institute of Aeronautics and Astronautics Paper AIAA-2005-4124

jet from flapping and limits the mixing in the chamber. Also, the grid refinement at the wall is an issue that can play an important role in heat flux prediction.

The second study focuses on the influence of thermodynamic and transport properties modeling on wall heat transfer in a high pressure three injector system. Comparisons between thermally perfect gas and real gas models are conducted and results show that the choice of the model is very important. Real gas formulation allows proper inlet flow conditions. Modifications of these conditions can have a large impact on the overall combustion dynamics and on the wall heat flux, even though the extent of the real gas effects is quite limited. The effect of pressure alone on the transport properties also changes the overall behavior, proving that the inclusion of real gas transport properties can be a first step towards better modeling of high pressure gas turbines or rocket engines.

Acknowledgments

References

[1] Cheng, G. and Farmer, R., "CFD spray combustion model for liquid rocket engine injector analyses," *AIAA 2002-0785*, 2002.

[2] Cheng, G., Johnson, C., Muss, J., and Cohn, R., "Swirl Coaxial Injector Development, Part II: CFD Modeling," 2002, JANNAF CS/APS/PSS/MSS Joint Meeting, Destin, FL.

[3] Cheng, G. and Farmer, R., "Development of efficient real-fluid model in simulating liquid rocket injector flows," *AIAA 2003-4466*, 2003.

[4] Zong, N., Wang, S., and Yang, V., "Cryogenic Fluid Jet Dynamics at Supercritical Conditions," *Proceeding of Third International Symposium on Turbulent and Shear Flow Phenomena, Sendai, Japan, June 2003*, 2003.

[5] Ierardo, N., Congiunti, A., and Bruno, C., "Mixing and Combustion in Supercritical O_2/CH_4 Liquid Rocket Injectors," 2004, 42nd Aerospace Sciences Meeting & Exhibit, Reno, Nevada, AIAA 2004-1163.

[6] Oefelein, J. C., "LES of Supercritical LOX-H2 Injection and Combustion in a Shear Coaxial Uni-Element Rocket," 2003.

[7] Oefelein, J. C., "Simulation of Combustion and Thermophysics in Practical Propulsion Systems," 2004, 42nd Aerospace Sciences Meeting & Exhibit, Reno, Nevada, AIAA 2004-0159.

[8] Fureby, C., "Large-Eddy Simulation of Turbulent Anisochoric Flows," *AIAA Journal*, Vol. 33, No. 7, 1995, pp. 1263–1272.

[9] Tramecourt, N., Amaya, J., and Menon, S., "LES of Supercritical Mixing and Combustion," *AIAA-2004-3381*, 2004.

[10] Kim, W.-W. and Menon, S., "A new incompressible solver for large-eddy simulations," *International Journal of Numerical Fluid Mechanics*, Vol. 31, 1999, pp. 983–1017.

[11] Nelson, C. C. and Menon, S., "Unsteady Simulations of Compressible Spatial Mixing Layers," *AIAA-98-0786*, 1998.

[12] Chakravarthy, V. K. and Menon, S., "Large-Eddy Simulations of Turbulent Premixed Flames in the Flamelet Regime," *Combustion Science and Technology*, Vol. 162, 2001, pp. 175–222.

[13] Wilke, C. R., "A Viscosity Equation for Gas Mixtures," *Journal of Chemical Physics*, Vol. 18, 1950, pp. 517–519.

[14] Wassiljewa, A., *Phyzik. Zeitung*, Vol. 5, 1904, pp. 737.

[15] Congiunti, A., Bruno, C., and Giacomazzi, E., "Supercritical Combustion Properties," 2003, 41st Aerospace Sciences Meeting & Exhibit, Reno, Nevada, AIAA 2003-0478.

[16] Miller, R. S., J., B., and Harstad, K., "Direct Numerical Simulations of Supercritical Fluid Mixing Layers applied to Heptane-Nitrogen," *J. Fluid Mech.*, Vol. 436, 2001, pp. 1–39.

[17] Chung, T. H., Ajlan, M., Lee, L. L., and Starling, K. E., "Generalized Multiparameter Corresponding State Correlation for Polyatomic, Polar Fluid Transport Properties," *Industrial and Chemical Engineering Research*, Vol. 27, 1988, pp. 671–679.

[18] Okong'o, N., Bellan, J., and Harstad, K., "Direct Numerical Simulations of O_2/H_2 Temporal Mixing Layers Under Supercritical Conditions," *AIAA Journal*, Vol. 40(5), 2002, pp. 914–926.

[19] Poinsot, T. and Veynante, D., Edwards, 2005.

[20] Drummond, J. P., Hussaini, M. Y., and Zang, T. A., "Spectral Methods for Modeling Supersonic Chemically Reacting Flowfields," *AIAA Journal*, Vol. 24(9), 1986, pp. 1461–1467.

[21] Spalding, D. B., "Mixing and Chemical Reaction in Steady Confined Turbulent Flames," *Thirteenth Symposium (International) on Combustion*, 1971, pp. 649–657.